




 Cite this: *RSC Adv.*, 2025, 15, 1792

2D V₂C MXene/2D g-C₃N₄ nanosheet heterojunctions constructed *via* a one-pot method for remedying water pollution through high-efficient adsorption together with *in situ* photocatalytic degradation†

 Shishan Xue, * Dengliang He,* Herong Zhang, Yuning Zhang, Yu Wang, Yurong Zeng, Shuxin Liu  and Ning Chen

With the development of modern industry, the problems of water pollution have become increasingly serious. There is a strong need to develop highly efficient and environmentally friendly technologies to address water pollution. In this work, a novel 2D V₂C MXene/2D g-C₃N₄ nanosheet heterojunction was constructed *via* a one-pot method. The obtained composite materials displayed excellent purifying capacity for dye pollutants, with removal ratios for crystal violet (CV), Rhodamine B (RhB) and methylene blue (MB) of 99.5%, 99.5%, and 95% within 80 min (including an adsorption process for 50 min and photodegradation process for 27 min), respectively. The extraordinary purifying capacity was accomplished through high-efficient adsorption together with *in situ* photocatalytic degradation within the unique 2D/2D heterojunction structure. The successful exploitation of 2D V₂C MXene/2D g-C₃N₄ nanosheet heterojunctions provided a simple method to efficiently remedy water pollution.

Received 8th October 2024

Accepted 7th January 2025

DOI: 10.1039/d4ra07222g

rsc.li/rsc-advances

1. Introduction

Nowadays, water pollution has become an extremely serious issue in modern society, greatly threatening economic growth and ecosystem health. Industrial water, especially dye waste water, which is primarily discharged by textile, printing, and electroplating industries, has attracted considerable attention due to its massive quantity and the difficulty in remediation.^{1,2} These high toxicity organic dyes can lead to carcinogenic, teratogenic, and mutagenesis effects on humans and aquatic organisms.³ In consequence, it is urgently required to eliminate contaminants from dye wastewater before it is discharged.

In the past decades, many water treatment technologies have been developed by researchers, including adsorption, flocculation, membrane separation, biological degradation, photocatalysis, and Fenton reaction.^{4–6} Among them, photocatalysis has attracted abundant attention due to the sustainable utilization of solar energy, which enables the conversion of solar energy into chemical energy to address water pollution issues.⁷ In recent years, semiconductors including BiVO₄, TiO₂, CdS, Bi₂WO₄ and non-metallic graphitic carbon nitride (g-C₃N₄) have

been extensively researched in various fields.^{8–11} g-C₃N₄, with a 2D sheet-like structure formed by the regular arrangement of tris-s-triazine units, displays numerous extraordinary features, such as nontoxicity, non-metallic composition and a narrow band gap.¹² However, bulk g-C₃N₄, fabricated through the thermal condensation of organic precursors containing both carbon and nitrogen, is restricted by low light adsorption and slow charge transfer rate of electron–hole pairs.¹³ Researchers working in this field have proposed many strategies to improve the photocatalysis activity, including introducing heteroatoms or nitrogen vacancies, coupling with other semiconductors, and controlling the morphology.¹⁴

Delaminating multi-layered bulk g-C₃N₄ to obtain g-C₃N₄ nanosheets is one of the most popular strategies for controlling morphology to improve the photocatalytic activity.¹⁵ Common methods to exfoliate bulk g-C₃N₄ include ultrasonic thinning, thermal oxidation peeling and acid-based chemical peeling.¹⁶ For instance, Lin *et al.* exfoliated bulk g-C₃N₄ into g-C₃N₄ nanosheets through an ultrasound method in ethanol/water, isopropanol/water and dimethylformamide/water with a concentration of 0.1–3 mg mL^{−1}. The specific surface area of the obtained g-C₃N₄ nanosheets was as high as 59.4 m² g^{−1}, which was five times that of bulk g-C₃N₄.¹⁷ Wan *et al.* exfoliated bulk g-C₃N₄ into ultrathin protonated g-C₃N₄ (PCN) nanosheets under the assistance of H₂SO₄, which exhibited improved photocatalytic activity.¹⁸ However, regulation and control of the structure of single-phase material to enhance the photocatalyst

Chemistry and Chemical Engineering School, Mianyang Teachers' College, Mianxing Road No. 166, Mianyang City, Sichuan Province, 621000, China. E-mail: xueshishancarol@163.com; 449011902@qq.com

† Electronic supplementary information (ESI) available. See DOI: <https://doi.org/10.1039/d4ra07222g>



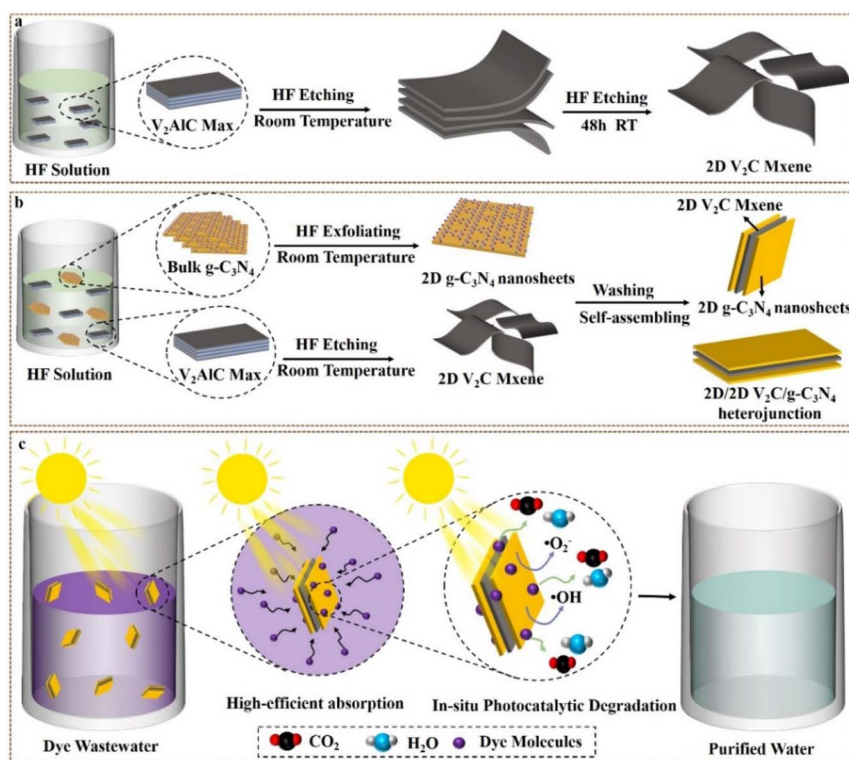
activity was finite, attributed to the recombination between electrons and holes within the single-phase material, thus largely impeding the photocatalytic reaction.¹⁹

Establishing heterojunction photocatalysts enables to settle these problems through accelerating the separation of electrons and holes and advancing the capacity of light adsorption.^{19,20} Zhu *et al.* constructed a novel Bi₂Sn₂O₇/g-C₃N₄ heterojunction through an ultrasound-assisted hydrothermal method, which decomposed 94% norfloxacin in the experimental solution and eliminated 89% of norfloxacin after five cycles, exhibiting outstanding stability and cyclability of photocatalytic activity.²¹ Zhao *et al.* synthesized a 2D/2D BiPO₄/g-C₃N₄-B nanosheet heterojunction photocatalyst with 97.3% degradation of RhB within 25 min under visible light.²² These works demonstrated that 2D layered material coupled with 2D g-C₃N₄ could improve the charge carrier separation efficiency, which is ascribed to the cations in the layered structure providing the charge trapping ability.²³

MXenes, as a novel family of 2D nanomaterials comprising transition metal carbides, nitrides, and carbonitrides, have stimulated considerable attentions in advancing the photocatalytic activity of semiconductor materials.²⁴ V₂C MXene, the newly explored layered material, manifests numerous distinguished properties including excellent electrical conductivity, high carrier mobility, and various active groups at the surface terminus, which possesses a greater specific surface area and more active centers compared to other MXenes, leading to promising application as a cocatalyst for pollutant

photodegradation.⁶ Sherryrna *et al.* exploited the novel V₂C MXenes-coupled g-C₃N₄ 2D/2D nanohybrids showing the remarkable yield of H₂ with a maximal rate of 360 mmol g⁻¹ h⁻¹, which was four times than that of pristine g-C₃N₄.²⁵ Tahir designed V₂C MXene combined with exfoliated g-C₃N₄, which enabled the reduction of CO₂ to CO with a yield rate of 9289 mmol g⁻¹ h⁻¹.²⁶ These published works convincingly demonstrated that constructing heterojunction photocatalysts enabled a prominent enhancement of the photocatalytic activity.

In this work, 2D V₂C MXene/2D g-C₃N₄ heterojunctions were successfully developed *via* a one-pot method in HF solution at room temperature, which almost completely purified the dye waste water under visible light through high-efficiency adsorption together with *in situ* photocatalytic degradation (Scheme 1). Compared to pristine g-C₃N₄, 2D V₂C MXene/2D g-C₃N₄ heterojunctions displayed higher charge transfer rate, better separation efficiency of photogenerated e⁻-h⁺ pairs, narrower band gap and greater adsorption ability of visible light, promoting the photodegradation of RhB, CV, and MB. The removal ratio (including adsorption and photodegradation processes) onto CV, RhB and MB reached 99.5%, 99.5%, and 95%, respectively, demonstrating that 2D V₂C MXene is a perfect cocatalyst with excellent performance to modify 2D g-C₃N₄ nanosheets. As we know, there is no report on the preparation of 2D V₂C MXene/2D g-C₃N₄ heterojunctions *via* the one-pot strategy. This work provided a profoundly simple path to synthesize 2D V₂C MXene/2D g-C₃N₄ heterojunctions with outstanding photocatalytic



Scheme 1 Schematic of the preparation process of (a) V₂C MXene and (b) 2D/2D V₂C/g-C₃N₄ heterojunction; (c) schematic of the purification process of dye wastewater using 2D/2D V₂C/g-C₃N₄ heterojunction.

activity, tremendously inspiring the preparation of high-activity photocatalysts. Meanwhile, this work is also important for remedying water pollution through high-efficiency adsorption together with *in situ* photocatalytic degradation.

2. Results and discussion

2.1 Morphological and structural analysis

2.1.1 X-Ray diffraction (XRD). The crystalline structure and existence of $g\text{-C}_3\text{N}_4$ components in the nanocomposites were confirmed by XRD. As shown in Fig. 1a, the typical peaks of $\text{V}_2\text{AlC Max}$ at 13.4° , 27.1° , 35.5° , 41.1° , 45.1° , 55.1° , 63.8° , 75° and 78.8° belonged to (002), (004), (101), (103), (104), (106), (110), (109) and (116) planes, respectively, demonstrating the hexagonal crystal structure of $\text{V}_2\text{AlC Max}$.^{27–29} The diffraction peaks at 13.4° , 35.5° , 41.1° , 55.5° , 63.8° , 75° and 78.8° , attributed to (002), (101), (103), (106), (110), (109) and (116), were observed in the XRD pattern of exfoliated $\text{V}_2\text{C MXene}$, in which 13.4° and 41.1° were weakened after etching by HF solution for 48 h, verifying the incomplete removal of Al atoms, while 75° and 78.8° coincided with the (109) and (116) crystal planes of $\text{V}_2\text{AlC Max}$, respectively, illustrating that $\text{V}_2\text{C MXene}$ nanosheets were fabricated from $\text{V}_2\text{AlC Max}$.^{30,31} Besides, the appearance of new characteristic peaks at 9.2° and 11.8° further confirmed the successful synthesis of $\text{V}_2\text{C MXene}$.³² The distinctive peaks at 12.8° and 27.5° in the $g\text{-C}_3\text{N}_4$ XRD pattern assigned to (100) and (002) crystalline planes indicated the $g\text{-C}_3\text{N}_4$ aromatic systems' interlayer structural packing and the distinctive interplanar stacking peak, verifying the successful production of $g\text{-C}_3\text{N}_4$ from urea precursor by thermal polycondensation.^{33,34} A slight shift from 27.1° to 27.6° (belonging to $\text{V}_2\text{C MXene}$) was observed after compositing with $g\text{-C}_3\text{N}_4$, attesting the variation of interlayer spacing, while the primary characteristic peaks all appeared without distinct shifting, demonstrating the efficient synthesis of both nanocomposite $\text{V}_2\text{C/g-C}_3\text{N}_4$ heterojunction, as evidenced by their effective interaction.³⁵

2.1.2 Fourier transform infrared (FT-IR). FT-IR was carried out to identify the molecular structures of the $\text{V}_2\text{C/g-C}_3\text{N}_4$ heterojunction and the interactions between $\text{V}_2\text{C MXene}$ and $g\text{-C}_3\text{N}_4$ nanosheets. As shown in Fig. 1b, the characteristic peak in the FT-IR spectrum of $g\text{-C}_3\text{N}_4$ at 814 cm^{-1} was assigned to the

triazine ring system, and the peaks in the region from 1100 to 1700 cm^{-1} originated from trigonal C-N(-C)-C (full condensation) and bridging C-NH-C units (partial condensation).^{13,36} For pristine $\text{V}_2\text{C MXene}$, the adsorption peaks at 983 cm^{-1} , 1594 cm^{-1} and 618 cm^{-1} were attributed to -C-F , -C=O and V-O vibrations, respectively. Besides, the characteristic peak at 2353 cm^{-1} belonging to V_2C was also observed in the spectrum.^{6,37,38} Notably, all the characteristic peaks belonging to both $g\text{-C}_3\text{N}_4$ and $\text{V}_2\text{C MXene}$ that appeared in the FT-IR spectrum of $\text{V}_2\text{C/g-C}_3\text{N}_4$ heterojunction with a slight shift were ascribed to the strong interactions between $\text{V}_2\text{C MXene}$ and $g\text{-C}_3\text{N}_4$. All the discoveries concluded that $\text{V}_2\text{C MXene}$ was successfully incorporated into the nanocomposite to yield the heterojunction.

2.1.3 Raman spectroscopy. Raman spectroscopy analysis is capable of determining rotational, vibrational and other low frequency patterns of heterojunctions. As shown in Fig. 1c, the Raman spectrum of $\text{V}_2\text{C MXene}$ displayed distinct peaks at 141 , 195 , 280 , 404 and 986 cm^{-1} , which were ascribed to Raman-active $\text{V}_2\text{C MXene}$ vibration mode. Additionally, the appearance of the peaks at 986 cm^{-1} , attributed to the enhancement of interlayer spading in $\text{V}_2\text{C MXene}$ and 404 cm^{-1} arising from the active vibration modes of the terminated $\text{V}_2\text{C MXene}$ confirmed the successful synthesis of $\text{V}_2\text{C MXene}$.^{35,39,40} However, the resolution of the recorded Raman spectra of $g\text{-C}_3\text{N}_4$ was fairly poor due to the fluorescence interference, while some weak characteristic peaks appeared at 207 , 353 , 482 , 576 , 739 , 961 , 1233 , 1307 cm^{-1} for bulk $g\text{-C}_3\text{N}_4$ corresponding to the vibrational modes of CN heterocycles (Fig. S1†).^{35,40,41} For the $\text{V}_2\text{C/g-C}_3\text{N}_4$ heterojunction, the distinct peaks weakened for $\text{V}_2\text{C MXene}$ compared to that of $\text{V}_2\text{C MXene}$, which was disturbed by the fluorescence of $g\text{-C}_3\text{N}_4$ on it. However, this phenomenon verified the successful combination of $g\text{-C}_3\text{N}_4$ and $\text{V}_2\text{C MXene}$ to establish the $\text{V}_2\text{C/g-C}_3\text{N}_4$ heterojunction.

2.1.4 X-ray photoelectron spectra (XPS). The elemental states of $\text{V}_2\text{C/g-C}_3\text{N}_4$ heterojunction, $g\text{-C}_3\text{N}_4$ and $\text{V}_2\text{C MXene}$ were determined by XPS, as shown in Fig. 2 S2 and S3,† respectively. As shown in Fig. S2,† obvious C, N and O peaks were exhibited in the XPS spectrum of $g\text{-C}_3\text{N}_4$, where the O peak was probably attributed to H_2O /oxidation-generated oxides adsorbed on the sample surface. C 1s spectra showed three

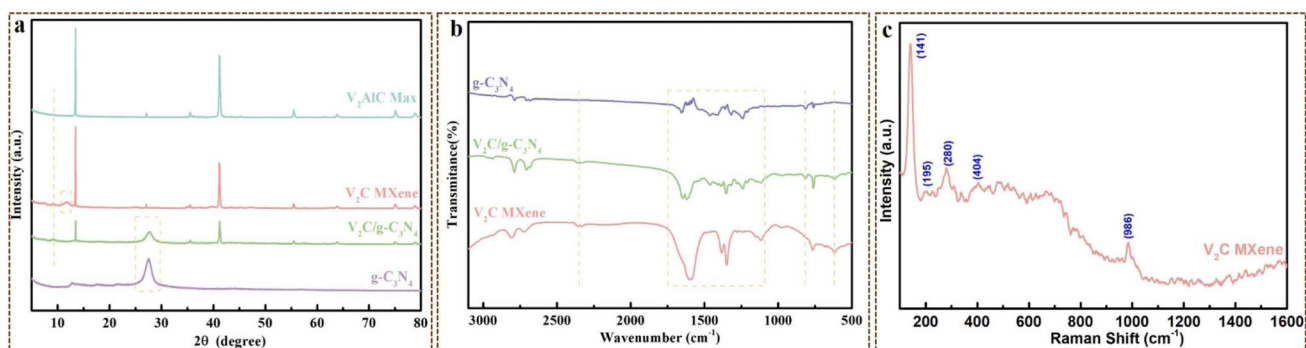


Fig. 1 (a) XRD patterns of $\text{V}_2\text{AlC Max}$, $\text{V}_2\text{C MXene}$, bulk $g\text{-C}_3\text{N}_4$ and $\text{V}_2\text{C/g-C}_3\text{N}_4$; (b) FT-IR spectra of $g\text{-C}_3\text{N}_4$, $\text{V}_2\text{C MXene}$ and $\text{V}_2\text{C/g-C}_3\text{N}_4$; Raman spectra of (c) $\text{V}_2\text{C MXene}$.

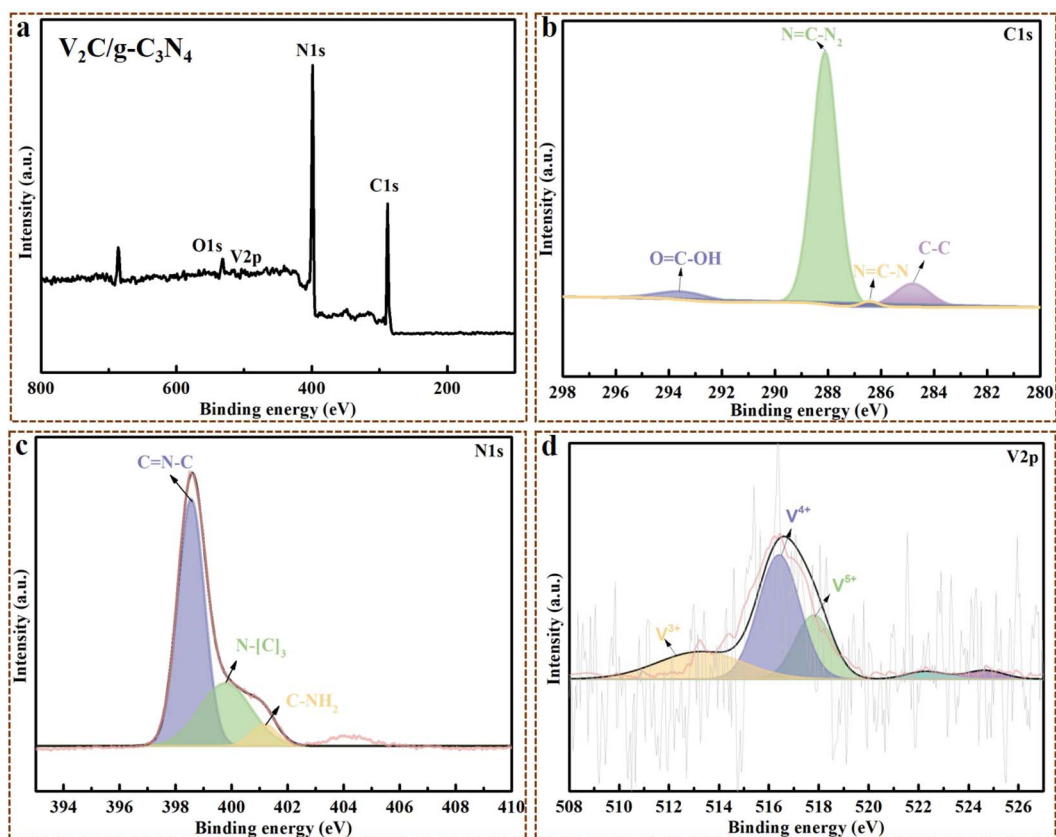


Fig. 2 XPS spectra of (a) $V_2C/g-C_3N_4$; (b) C 1s; (c) N 1s; (d) V 2p.

different chemical states corresponding to sp^3 C–N=C, O–CN and C–C at 288.1 eV, 286.2 eV and 284.8 eV, respectively. The N 1 s spectrum displayed the typical features of $g-C_3N_4$, with 398.6 eV (C–N=C), 401.0 eV (C–NH₂) and 404.6 eV ascribed to sp^2 -hybridized N, amino, and excitation, respectively.^{41,42} For pristine V_2C MXene, C, V, O and Al peaks were distinctly displayed in the XPS spectra, where Al peaks were weak, certifying that Al were almost completely etched away from V_2AlC Max (Fig. S3†).⁴³ The five peaks that appeared in the V 2p spectrum correspond to different oxidation states of V, where 513.3 eV, 514.2 eV, 516.6 eV, 521.2 eV and 522.8 eV were contributed by V^{2+} , V^{3+} , V^{4+} , V–C bond and their doublets, respectively.^{26,44} The spectrum in the C 1s region well fitted the peaks of 282.3 eV, 284.8 eV, 286.3 eV and 288.2 eV that originated from C–V, C–C, C–O and O–C=O, respectively, while the peaks in the O 1 s region located at 529.6 eV, 531.7 eV and 533.8 eV originated from V–O, V–C–O and OH[−], respectively.⁴⁴ For the $V_2C/g-C_3N_4$ heterojunction, C, N, V, and O peaks were all observed in the XPS spectrum (Fig. 2a), where the O peaks were possibly attributed to the presence of oxygen vacancies and hydroxyl group. As shown in Fig. 2b, the remarkable peaks at 284.8 eV, 286.4 eV, 288.1 eV and 293.6 eV were derived from C–C, N=C–N, N=C–N₂ and O=C–OH, respectively, which was in accordance with the C 1s spectrum of $g-C_3N_4$ and V_2C MXene without a distinct shift. Three binding energy peaks in the N 1 s spectrum (Fig. 2c) at 398.5 eV (C=N–C), 399.8 eV (N–[C]₃) and 401.1 eV (C–NH₂) were ascribed to sp^2 -hybridized N, graphitic N

and amino, respectively, which was highly consistent with the XPS results of $g-C_3N_4$ and V_2C MXene. The V 2p spectra displayed five peaks at 513.2 eV, 516.4 eV, and 517.8 eV belonging to V^{3+} , V^{4+} , and V^{5+} with their doublets at 522.3 eV and 524.6 eV (Fig. 2d). All the XPS results of the $V_2C/g-C_3N_4$ heterojunction, $g-C_3N_4$ and V_2C MXene revealed that the 2D/2D V_2C MXene/ $g-C_3N_4$ nanosheets heterojunctions were successfully developed in this work without damaging the pristine elemental states of $g-C_3N_4$ and V_2C MXene.

2.1.5 SEM and EDX analysis. The microstructures of $g-C_3N_4$, V_2AlC Max, V_2C MXene and $V_2C/g-C_3N_4$ heterojunction are displayed in Fig. 3 and S4† surveyed by SEM. As shown in Fig. S4a,† the sheets-like structure of $g-C_3N_4$ was observed while the sheets exhibited distinct agglomeration. However, after etching by HF solution, the bulk $g-C_3N_4$ was exfoliated to nanosheets, displaying the 2D nanostructure. The tight layered structures of V_2AlC Max constituted by boards and compacted sheets is shown in Fig. S4b,† which was linked through metallic bonds, generating the infinitesimal interlayer spacing. V_2C MXene showed a 2D structure after etching with HF solution for 48 h, exhibiting the unconsolidated layered structure which enabled to establish the interactions between other 2D materials such as 2D $g-C_3N_4$ (Fig. 3a). Intriguingly, the successful synthesis of 2D/2D $V_2C/g-C_3N_4$ heterojunctions through the one-pot etching method was certified by the SEM image, in which 2D $g-C_3N_4$ nanosheets growing on 2D V_2C MXene increased the interfacial contact area for charge carrier migration (Fig. 3c).

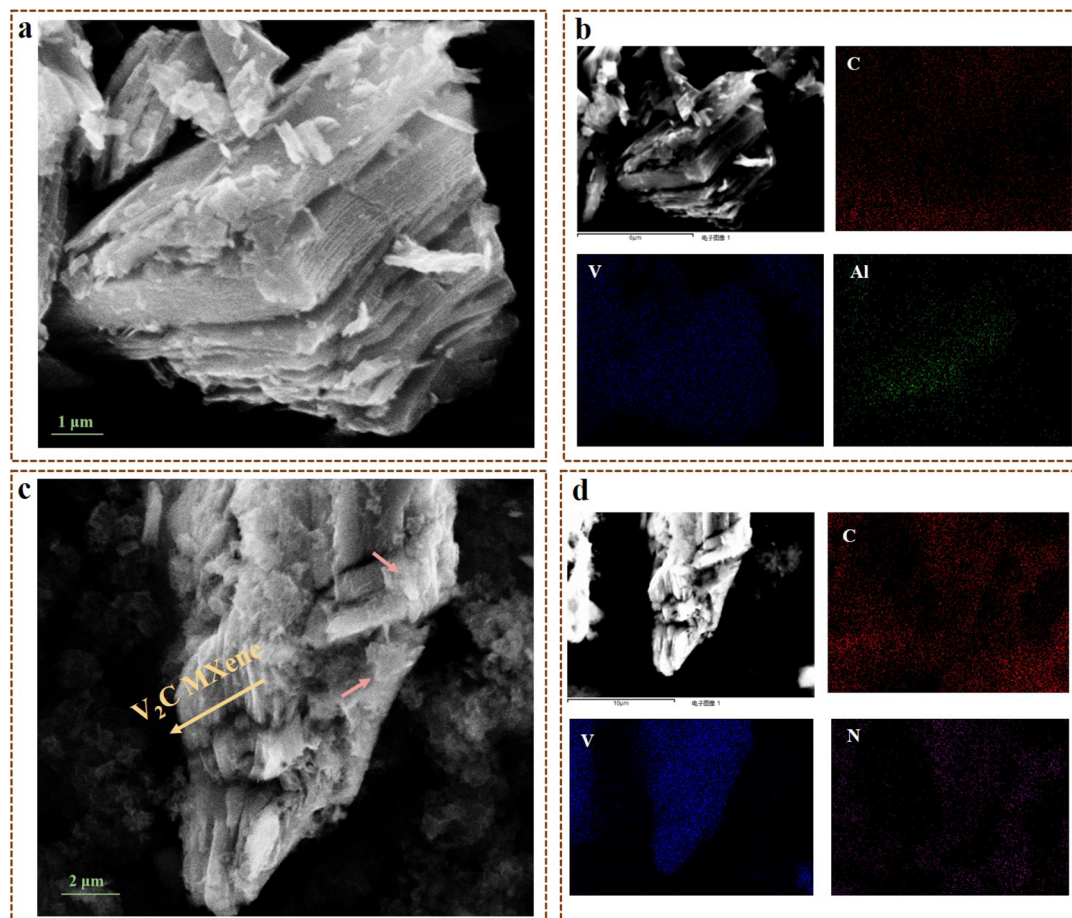


Fig. 3 (a) SEM image of V_2C MXene and (b) corresponding EDX mapping of V_2C MXene; (c) SEM image of V_2C MXene $V_2C/g-C_3N_4$ heterojunction and (d) corresponding EDX mapping of the V_2C MXene $V_2C/g-C_3N_4$ heterojunction.

The compact contact between 2D $g-C_3N_4$ nanosheets and 2D V_2C MXene led to the production of more electron transport routes, contributing to electron transport and separation.

EDX mapping analysis was performed to investigate the distribution of elements in the samples (Fig. 3b, d, S4b and d†). The presence of all elements in $g-C_3N_4$, V_2C MXene and $V_2C/g-C_3N_4$ heterojunctions was confirmed by the EDX plots in Fig. S5.† V and Al were observed in the plots of V_2C MXene and $V_2C/g-C_3N_4$ heterojunctions, while N appeared in the plots of $g-C_3N_4$ and $V_2C/g-C_3N_4$ heterojunctions. The existence of main elements in the samples was also supported by the EDX mapping images. In $g-C_3N_4$, the main elements were C, N, and O, while the appearance of Au was attributed to the gold-spraying process on the sample (Fig. S4 and S5†). C, V, Al, and F were observed in V_2C MXene, verifying the etching process on V_2AlC by HF to remove Al, generating V_2C MXene. All the elements in both $g-C_3N_4$ and V_2C MXene appeared in the EDX mapping of the $g-C_3N_4/V_2C$ heterojunction, which determined the hybrid of $g-C_3N_4$ and V_2C MXene. Finally, the $g-C_3N_4/V_2C$ heterojunction was synthesized with a high degree of purity due to the presence of the predicted elements in $V_2C-g-C_3N_4$ photocatalysts.

2.1.6 BET analysis. The specific surface area of V_xG_y was verified by Brunauer–Emmett–Teller (BET) analysis. As shown

in Fig. 4a, the N_2 adsorption–desorption isotherms of V_2AlC Max, V_2C MXene, $g-C_3N_4$ and $V_2C/g-C_3N_4$ heterojunction are presented, which showed type IV isotherms with distinct H_3 hysteresis loop, according to IUPAC classification.⁴⁵ These phenomena coincided with the characteristic of solids with micro- and mesopores and orderly macropores containing narrow mesopores interconnecting channels, certifying the mesoporous structure of the as-prepared materials.⁴⁶ Compared to V_2C MXene, the hysteresis loop area of the $V_2C/g-C_3N_4$ heterojunction greatly magnified, which is attributed to the production of abundant mesopores generated from the recombination of V_2C MXene and $g-C_3N_4$.⁴⁷ Besides, the specific surface area of V_2AlC Max, V_2C MXene, $g-C_3N_4$ and $V_2C/g-C_3N_4$ heterojunction was calculated as 0.102, 7.135, 115.636 and 70.122 $m^2 g^{-1}$, respectively (Table S1†). The average pore diameter of V_2AlC Max, V_2C MXene, $g-C_3N_4$ and $V_2C/g-C_3N_4$ heterojunction was calculated through the Barrett–Joyner–Halenda (BJH) method as 10.86, 13.94, 9.09 and 14.64 nm, respectively (Fig. S6 and Table S1†), demonstrating the existence of mesopores on these materials. Remarkably, the specific surface area and the pore volume of the $V_2C/g-C_3N_4$ heterojunction was much higher than that of the V_2C MXene, which indicated that $g-C_3N_4$ was successfully intercalated in V_2C MXene, thus enlarging the interlamellar spacing and providing

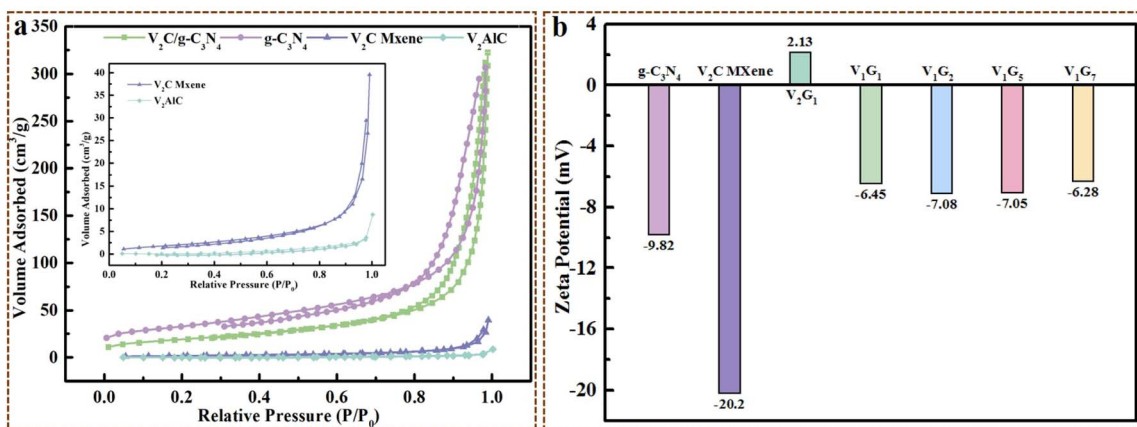


Fig. 4 (a) N₂ adsorption–desorption isotherms of V₂AlC Max, V₂C MXene, g-C₃N₄ and V₂C/g-C₃N₄ heterojunction; (b) zeta Potential of g-C₃N₄, V₂C MXene and V_xG_y heterojunctions.

affluent active sites to enhance the photocatalytic activity.³⁴ Thus, the intercalation of g-C₃N₄ in the V₂C MXene highly advanced the specific surface area and pore volume, which was vital to boost the photocatalytic property.

2.1.7 Zeta potential. The investigation of the surface electrical behaviour of materials is crucial to understand the adsorption behaviour onto dye molecules. Zeta potential studies enabled to reflect the surface charge performance of the materials to parse the interactions between g-C₃N₄ and V₂C MXene and comprehend the adsorption behaviour of different dye pollutants. As shown in Fig. 4b, the zeta potential of bulk g-C₃N₄ and V₂C MXene was measured to be -9.8 mV and -20.2 mV, respectively, demonstrating that the materials carried the negative charges on their surface. Many published works demonstrated that g-C₃N₄ would be protonized through etching by acid, even the surface charge of which would transform to positive.^{48,49} The different surface charge performance illustrated that g-C₃N₄ and V₂C MXene bound with each other through electrostatic interaction. More crucially, the zeta potential of V₂G₁ heterojunction was 2.13 mV, showing electropositivity. It was supposed that the appropriate conjunction ratio within V₂G₁ between protonized g-C₃N₄ and V₂C MXene transformed the surface potential to positive. However, V₁G₁, V₁G₂, V₁G₃ and V₁G₇ heterojunctions were negative, and the results of their zeta potential are very close.

2.2 Band gap and optoelectronic characterization

2.2.1 Photoluminescence analysis. The optical characteristics of V₂C/g-C₃N₄ heterojunction were discerned by photoluminescence (PL) analysis, which enabled to elucidate the surface oxygen vacancies and the separation of photogenerated charges to evaluate the segregation and transfer performance of photogenerated charge carriers. The peaks were observed with visual wavelengths between 400 and 500 nm for g-C₃N₄ and V₂C/g-C₃N₄ heterojunction, while the PL peak of V₂C MXene barely appeared, attributed to its dark color (nearly black) reducing electron generation, indicating that the wavelength of both g-C₃N₄ and V₂C/g-C₃N₄ heterojunction has remarkable effects on PL spectral emission (Fig. 5a).⁵⁰ Moreover, the lower intensity

peak of V₂C MXene was observed, ascribed to its metallic property, which could barely generate electron–hole pairs.⁵¹ Generally, lower density and depressed emission peak manifested the efficient separation of e⁻ and h⁺, resulting in better photocatalytic activity. As shown in Fig. 5a, g-C₃N₄ displayed the highest PL peak owing to the band–band PL signal phenomenon generated by excitonic PL caused by n- π^* electronic transitions containing lone pairs of nitrogen atoms in g-C₃N₄, verifying the existence of sub gap flaws in g-C₃N₄.⁵¹ However, after coupling with V₂C MXene, the intensity of PL peaks sharply decreased, contributing to the more excellent charges separation proficiency, which meant more photocatalytic activity, ascribed to the introduction of V₂C that traps electron, facilitating charge transport over the interface between 2D V₂C MXene and 2D g-C₃N₄ nanosheets and resulting in the decreasing rate of recombination.^{52,53} More importantly, the superb separation efficiency of photogenerated e⁻-h⁺ pairs created by the interfaces between 2D V₂C MXene and 2D g-C₃N₄ nanosheets gave rise to the lowest excitation intensity of the V₂C/g-C₃N₄ heterojunction, illustrating that the metal-like nature of V₂C MXene as a mediator coupled with g-C₃N₄ dramatically accelerated the separation of photogenerated charge carriers and alleviated the photogenerated recombination e⁻-h⁺ pairs, which was beneficial to boost the photo-degradation efficiency of dye pollutants.

2.2.2 Electrochemical impedance spectra. Electrochemical impedance spectra (EIS) of g-C₃N₄, V₁G₅ heterojunction and V₁G₇ heterojunction obtained under visible light and dark environment are shown in Fig. 5b and S7,[†] respectively. Notoriously, the smaller arc radius means the smaller impedance of charge transfer, leading to a higher charge transfer rate of the materials.^{54–56} As shown in Fig. 5b, under visible light, the V₁G₅ heterojunction exhibited the smallest arc radius, while g-C₃N₄ showed the largest arc radius, which illustrated that the addition of V₂C MXene largely improved the efficiency of photogenerated carrier separation and the interfacial charge transfer potential. It was demonstrated that the extraordinary 2D/2D heterojunction structure showed high charge separation capacity, which remarkably advanced the efficiency of electron/

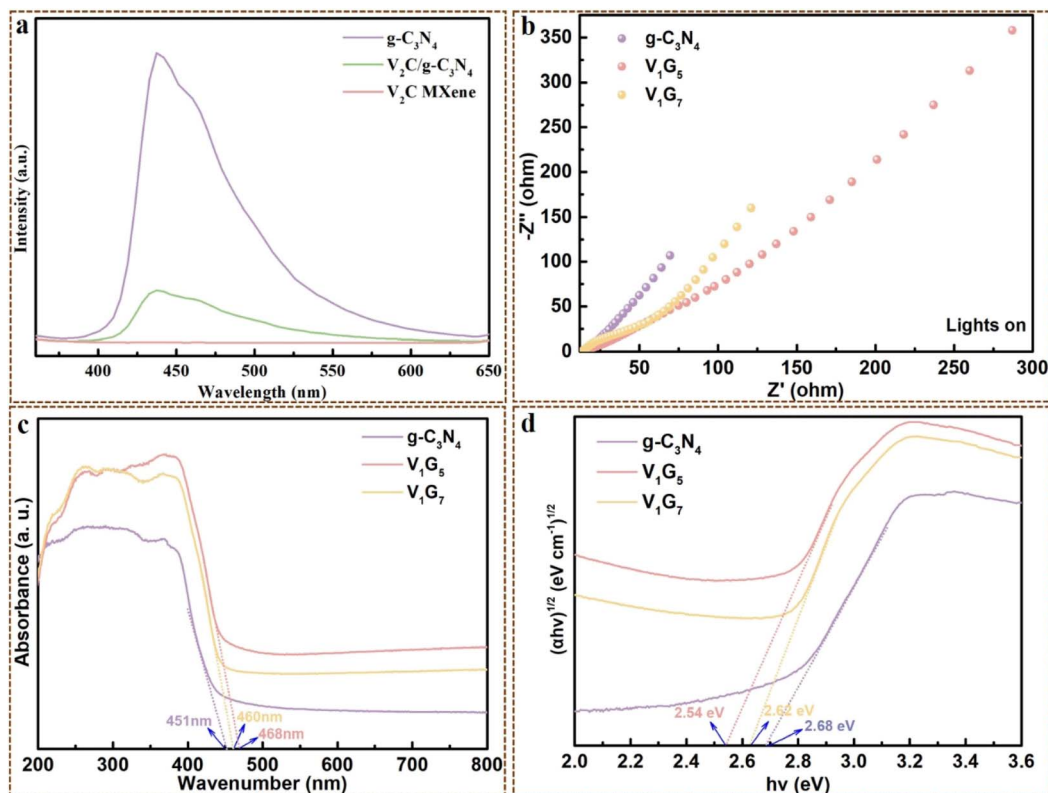


Fig. 5 (a) PL spectra of V_2C MXene, $g-C_3N_4$ and $V_2C/g-C_3N_4$ heterojunction; (b) electrochemical impedance spectra (under visible light); (c) UV-vis diffuse reflectance spectra (DRS); (d) Tauc-function band gap simulations of $g-C_3N_4$, V_1G_5 and V_1G_7 heterojunctions.

hole pair separation and transfer within the V_1G_5 heterojunction. However, the excessive addition of V_2C MXene to the heterojunction enlarged the arc radius, obstructing the charge transfer. Interestingly, under a dark environment, with the increase in the V_2C MXene contents, the arc radius lessened, which is probably owing to the MXene that enabled to trap electrons.^{57–59} Moreover, the PL spectra further verified that the V_xG_y heterojunction manifested significant photocatalyst activity after exposing to visible light (450–800 nm), which corresponded with the results of electrochemical impedance spectroscopy.

2.2.3 UV-vis diffuse reflectance spectra. UV-vis diffuse reflectance spectra (DRS) were carried out to understand the light absorption behaviour of the samples. The adsorption spectra of $g-C_3N_4$, V_1G_5 and V_1G_7 heterojunctions are shown in Fig. 8c. The absorption edges of $g-C_3N_4$, V_1G_5 and V_1G_7 were apparently observed at about 450 nm, which was in the blue region of the visible spectrum. Compared with $g-C_3N_4$, V_1G_5 and V_1G_7 heterojunctions displayed enhanced light absorption behavior in both ultraviolet and visible regions, ascribed to the broadband adsorption of V_2C MXene across the solar spectrum.⁶ Moreover, the absorbance of the V_1G_5 heterojunction was almost 10 times than that of $g-C_3N_4$ within the visible light region (450–800 nm) (Fig. 5c). The enhancement of light absorption capacity offered a higher photothermal effect to foster the photocatalytic reaction.^{51,60} However, the absorbance of the V_1G_7 heterojunction across the solar spectrum was slightly weaker than that of the V_1G_5 heterojunction, which

demonstrated that the excessive proportion V_2C MXene in the V_xG_y heterojunctions was detrimental to the absorption capacity for solar light. Further analysis of energy bandgap was performed to evaluate the optical performances of these samples. The bandgaps of $g-C_3N_4$, V_1G_5 heterojunction and V_1G_7 heterojunction simulated by Tauc-function model were 2.68 eV, 2.54 eV and 2.62 eV, respectively (Fig. 5d). Thereinto, the V_1G_5 heterojunction possesses the narrowest bandgap (2.54 eV), which means it enables the absorption of the greatest range of wavelengths in the visible spectrum, leading to the best photocatalytic activity.

2.3 Adsorption behaviour

The adsorption behaviour of V_xG_y was explored through the adsorption tests in different dye solutions (CV, RhB and MB) with the same original content of 20 mg L^{-1} at different pH values (pH = 4, 7 and 10). The adsorption capacity (Q_t , mg g^{-1}) of V_xG_y to all kinds of dyes at different pH values rapidly increased in the first 60 min and reached equilibrium after 100 min (Fig. S8†). As shown in Fig. 6a, the adsorption ratios (AR) of V_xG_y to CV were above 90% within 170 min, which was much higher than that of V_xG_y to RhB and MB, attributed to the smaller molecules of CV. With the increase in the $g-C_3N_4$ contents, the AR to CV ratio slightly changed in acidic environment, presenting the tendency to decline and then rise, while dramatic fluctuations of AR were observed in the neutral and alkaline environment. showing the same trend as that in

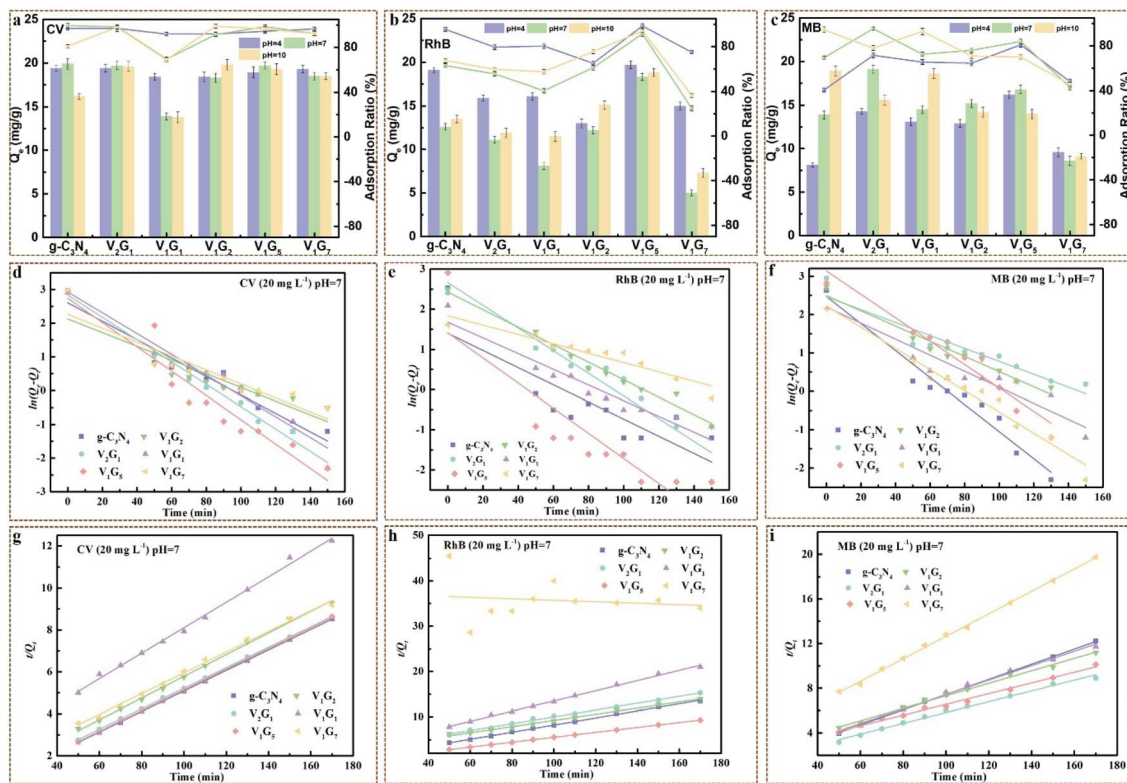


Fig. 6 Q_e and the adsorption ratio of (a) CV, (b) RhB and (c) MB at equilibrium in different pH environment onto V_xG_y heterojunctions; Adsorption kinetics for the adsorption of (d) CV, (e) RhB and (f) MB at pH value of 7 onto V_xG_y heterojunctions fitted by the pseudo-first-order kinetic model; adsorption kinetics for the adsorption of (g) CV, (h) RhB and (i) MB at pH value of 7 onto V_xG_y heterojunctions fitted by the pseudo-second-order kinetic model.

acidic environment. According to the results of zeta potential (Fig. 4b), V_xG_y protonized in acid solution, while more ionized in basic solution, which means that the adsorption ratios of V_xG_y in basic solution would be much better than that in acidic solution. However, the results of the adsorption experiments did not coincide with the supposition. For RhB, the AR in the solution with pH value of 4 was distinctly higher than that in the solution with pH value of 7 and 10. Thus, the pK_a of RhB was highly related to the adsorption results. It is known that the pK_a of RhB is 3.2. When the pH value was low, $-\text{COOH}$ on RhB barely ionized, leading to a positive charge on RhB, which was beneficial to the adsorption process. With increasing pH value, $-\text{COOH}$ on RhB gradually ionized until it was transformed to a zwitterion establishing dimer RhB molecules, which hardly entered the V_xG_y , thus impeding the adsorption process.⁶¹ On the other hand, the discrepancy of AR was highly dependent on the contents of $g\text{-C}_3\text{N}_4$ owing to the surface potential and occupation of adsorption sites of V_xG_y . Interestingly, the AR of V_1G_5 to CV, RhB and MB was much higher than that of other samples and barely affected by the pH value of the dye solutions, which is probably attributed to the appropriate conjunction ratio between V_2C MXene and $g\text{-C}_3\text{N}_4$ nanosheets, leading to the exposure of more adsorption sites and feasible surface potential.

The adsorption data of CV, RhB and MB by V_xG_y heterojunctions at different pH environment were analyzed by pseudo-

first-order kinetic model and pseudo-second-order kinetic model, respectively. The linear fitting lines and the corresponding kinetic parameters are shown in Fig. 6d–i, S9–S10 and Table S2–S10.[†] Remarkably, the adsorption process of CV, RhB and MB by the V_xG_y heterojunctions at different pH environment were all well simulated by the pseudo-second-order kinetic model with most of the correlation coefficients (R^2) ≥ 0.99 , while the R^2 of the pseudo-first-order kinetic model was below 0.95 at even about 0.6 (Tables S2–S10[†]), illustrating that the adsorption processes were dominantly depended on chemisorption. For the adsorption process of CV by V_xG_y heterojunctions at pH 4, most of the R^2 values of the pseudo-second-order kinetic model were above 0.99, while the R^2 of the pseudo-second-order kinetic model adsorbed by V_1G_5 was about 0.95, possibly affected by the interactions between V_2C MXene and $g\text{-C}_3\text{N}_4$. When the pH value improved to 7, all the R^2 of pseudo-second-order kinetic model were above 0.99, while the R^2 of pseudo-second-order kinetic model were above 0.99 at pH value of 10, except that of V_1G_1 , further demonstrating that the ratio of V_2C MXene and $g\text{-C}_3\text{N}_4$ and pH value of the environment simultaneously impacted the surface potentials of V_xG_y heterojunctions, leading to the transformation of predominance of adsorbing type and mechanism. Interestingly, the R^2 of pseudo-second-order kinetic model was above 0.99 during the adsorption process by V_xG_y heterojunctions when the dye solutions (CV, RhB and MB) were adsorbed at pH 7,

illustrating that the adsorption processes by V_xG_y heterojunctions were dominated by chemisorption when the influences of acidity and alkalinity were eliminated. The chemisorption including electrostatic and hydrogen bonds between adsorbent and adsorbates guaranteed that the dye molecules are hardly desorbed from V_xG_y heterojunctions rinsed in pure water. The electrostatic interaction was easily influenced by the pH of the dye solutions, further confirming the characteristics of the adsorption behaviours of V_xG_y heterojunctions at different pH values.

On the other hand, the original concentrations of dye solutions were also highly relevant to the adsorption behavior of V_xG_y heterojunctions. As shown in Fig. 7, with the increase in the original contents of dye solutions (CV, RhB and MB), the adsorption capacities at equilibrium increased, while the adsorption ratios decreased. V_1G_5 exhibited excellent adsorption property with adsorption ratio onto CV and RhB of 99.6% and 94%, respectively, while the adsorption ratio onto MB was only 66%. This was because MB has the lowest pK_a among the three dyes, leading to the largest differentials between it and the pH value (pH = 7), which means the least number of cationic functional groups on MB.^{48,62} Notably, the original contents of dye solutions greatly influenced the adsorption capacity at equilibrium. When the original content of CV was 15 mg L^{-1} ,

the Q_e of CV onto V_1G_5 was 14.4 mg g^{-1} , while the Q_e of CV onto V_1G_5 improved to 19.7 and 24.9 mg g^{-1} when the original contents of CV solution increased to 20 mg L^{-1} and 25 mg L^{-1} , respectively. The same phenomena were also observed in RhB and MB solutions, verifying the excellent adsorption property of V_xG_y heterojunctions.

The adsorption data onto CV, RhB and MB with different original contents onto V_xG_y heterojunctions were fitting by the pseudo-first-order kinetic model and pseudo-second-order kinetic model (Fig. 7d–i and S12†). Analogously, the R^2 of the pseudo-second-order kinetic model was much higher than that of the pseudo-first-order kinetic model during the adsorption process by V_xG_y heterojunctions when the dye solutions (CV, RhB and MB) had different original contents ($15, 20, 25 \text{ mg L}^{-1}$) at a pH value of 7, further confirming that the adsorption process is primarily based on chemisorption (Tables S11–S16†). It was clear that the R^2 of both pseudo-first-order kinetic model and pseudo-second-order kinetic model is barely related to the original contents of the dye solution. Notably, with increasing original contents of dye solutions, the adsorption rate was prominently boosted probably owing to the higher differential concentration. In addition, $Q_{e, \text{exp}}$ obtained through adsorption experiments and $Q_{e, \text{cal}}$ calculated through (E-7) were close to each other, illustrating that the adsorption processes were

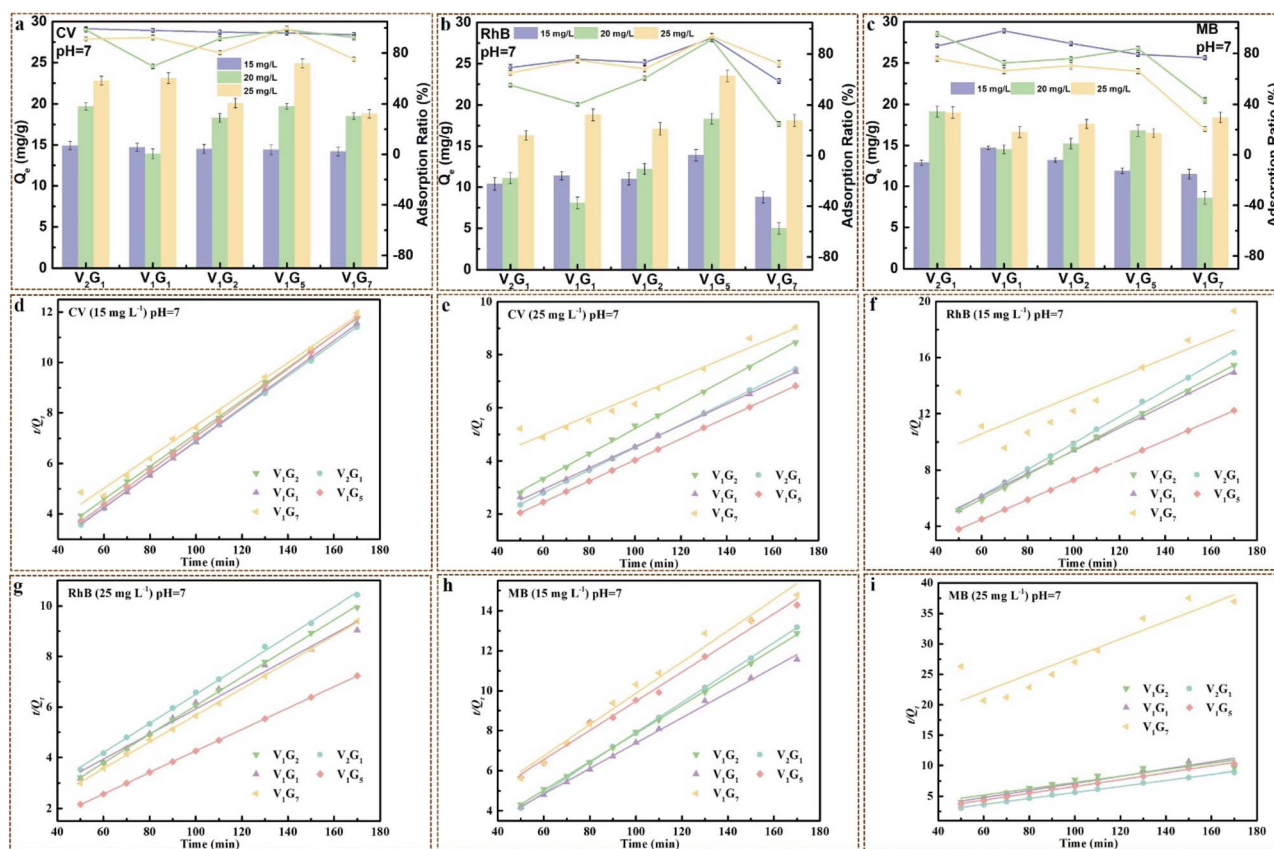


Fig. 7 Q_e and the adsorption ratio of (a) CV, (b) RhB and (c) MB at equilibrium with different original contents at pH 7 onto V_xG_y conjunctions; adsorption kinetics on the adsorption of CV with original contents of (d) 15 mg L^{-1} and (e) 25 mg L^{-1} ; RhB with original contents of (f) 15 mg L^{-1} and (g) 25 mg L^{-1} ; MB with original contents of (h) 15 mg L^{-1} and (i) 25 mg L^{-1} at pH 7 onto V_xG_y heterojunctions fitted by the pseudo-second-order kinetic model.

wonderfully simulated by pseudo-second-order kinetic model (Tables S11–S16†). For instance, the $Q_{e, \text{exp}}$ of V_1G_5 onto CV (25 mg L^{-1} , $\text{pH} = 7$) was 24.9 mg g^{-1} , while $Q_{e, \text{cal}}$ of V_1G_5 onto CV (25 mg L^{-1} , $\text{pH} = 7$) was 25.05 mg g^{-1} .

2.4 Photodegradation performance

The photodegradation performances of V_xG_y heterojunctions were investigated for CV, RhB and MB at different pH values with different initial concentrations under the visible light supplied by a metal halide lamp (50 W). As shown in Fig. 8a–c, the removal ratios of V_1G_5 heterojunctions for CV at pH value of 4, 7 and 10 were 95%, 99.5% and 98%, respectively, within 80 min (adsorption in dark environment for 50 min and then irradiation under visible light for 27 min), which was much higher than that of pure $g\text{-C}_3\text{N}_4$. In addition, the removal ratios of the V_1G_5 heterojunction for RhB at different pH values were all above 90%, while for MB, they were just about 80%. On the other hand, the removal ratios of the V_1G_5 heterojunction for CV with different original contents of 15, 20 and 25 mg L^{-1} at pH 7 were 98%, 99.5% and 96%, respectively, illustrating that the original contents of CV barely influence the purifying capacity of heterojunctions (Fig. S13†). Remarkably, the removal ratios of the V_1G_5 heterojunction for RhB with different original contents of 15, 20 and 25 mg L^{-1} at pH 7 were 96.6%, 92% and 98.8%, respectively, further certifying the extraordinary

purifying capacity of the V_1G_5 heterojunction for dye wastewater (Fig. S13†). However, the removal ratios of heterojunctions for MB were much lower than that of CV and RhB within 80 min, ascribed to the final removal ratio dependent on the two processes of adsorption and photodegradation, whereas the adsorption ratios of MB onto the heterojunctions were much lower than that of CV and RhB, resulting in the same surface potential between the heterojunctions and MB. However, the removal ratios of the V_2G_1 heterojunction for MB reached 99.3% when the irradiation time was prolonged to 90 min (total time of 140 min), which means that the photodegradation process enabled to nearly completely remove MB molecules. The adsorption and photocatalysis by the V_1G_5 heterojunction conjointly disposed dye wastewater, exhibiting the high-efficiency disposal capacity, which enabled the almost thorough removal of dye molecules within 80 min including an irradiation time of only 27 min.

3. Proposed mechanism for purifying water pollution

3.1 Proposed mechanism for adsorption behaviour

Based on the characteristics of adsorption of V_xG_y heterojunctions onto different dyes and combined with the results of BET analysis, zeta potential, adsorption behaviour and

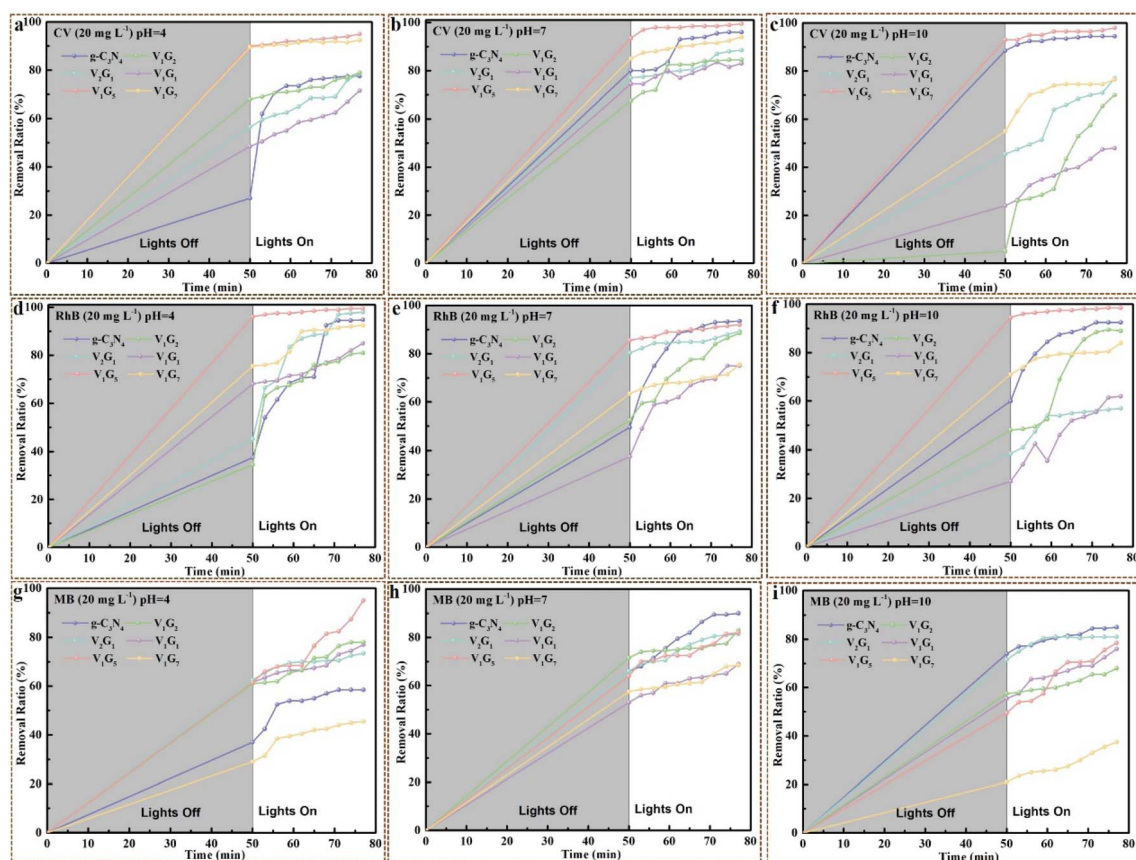
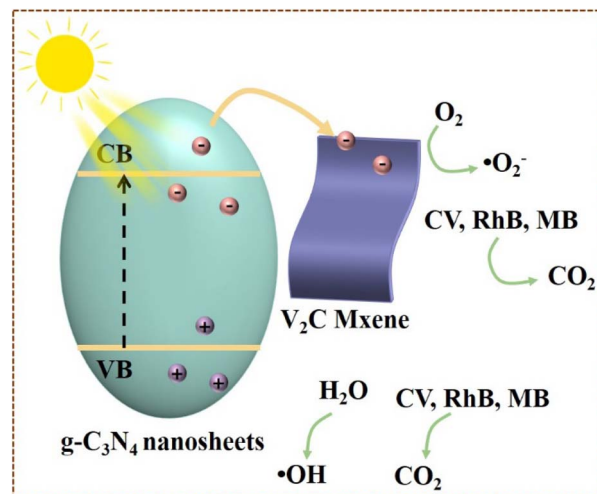


Fig. 8 Removal ratio of V_xG_y heterojunctions for CV (original content of 20 mg L^{-1}) at (a) pH = 4, (b) pH = 7, (c) pH = 10; for RhB (original content of 20 mg L^{-1}) at (d) pH = 4, (e) pH = 7, (f) pH = 10; for MB (original content of 20 mg L^{-1}) at (g) pH = 4, (h) pH = 7, (i) pH = 10.

adsorption kinetics fittings, the mechanism of adsorption behaviour of V_xG_y heterojunctions was proposed in this work. According to the results of BET analysis, $g\text{-C}_3\text{N}_4$ possessed the largest specific surface area among all the samples while the Q_e of $g\text{-C}_3\text{N}_4$ onto dyes is not the highest one. Obviously, the specific surface area of the $V_2C/g\text{-C}_3\text{N}_4$ heterojunction was smaller than that of $g\text{-C}_3\text{N}_4$, while the Q_e and adsorption ratio at equilibrium for the $V_2C/g\text{-C}_3\text{N}_4$ heterojunction were much higher than that of pristine $g\text{-C}_3\text{N}_4$, illustrating that the adsorption process scarcely depended on physical adsorption through mesopores within the materials. It was also confirmed by the fitting results of the first-order kinetic model (Fig. 6 and 7). The results of zeta potential further corroborated this supposition. As shown in Fig. 4b, all the samples exhibited electronegativity except the V_2G_1 heterojunction, while CV, RhB and MB were all cationic dyes, which means that chemisorption dominated the whole adsorption process. This supposition is also notarized by the coinciding fitting results of the second-order kinetic model, R^2 is above 0.99 (Fig. 6, 7 and Tables S2–S10†).

3.2 Proposed mechanism for photocatalytic degradation

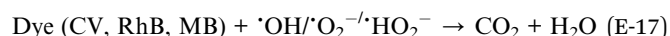
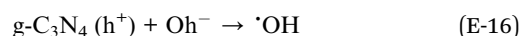
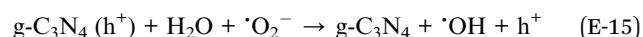
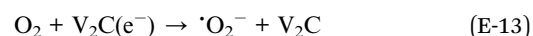
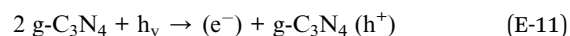
Based on the series characterizations and experiments, the photocatalytic mechanism was proposed to interpret the photocatalytic process of $V_2C/g\text{-C}_3\text{N}_4$ heterojunctions on CV, RhB and MB. PL and DRS analysis revealed that V_2C MXene could barely generate e^- and h^+ and hardly recombine e^- and h^+ pairs. These findings indicated that $g\text{-C}_3\text{N}_4$ was the main photocatalyst responsible for the electron–hole pairs generation, while V_2C MXene worked as a metallic conductor to expedite the photoreaction. This was the possible mechanism of charge transfer of heterojunctions that we supposed. According to the reported work, eqn (E10)–(E17) display the conversion and establishment of different active groups of $V_2C/g\text{-C}_3\text{N}_4$ heterojunctions throughout photocatalytic degradation onto dyes.^{63,64} Scheme 2 describes the process of generating photocarriers by $g\text{-C}_3\text{N}_4$. The e^- and h^+ were generated at the VB of $g\text{-C}_3\text{N}_4$ under visible light. The charge separation of photogenerated charges occurred, where e^- are excited to CB while h^+ remained in the VB (E-11). The shift of C 1s, N 1s and V 2p in $V_2C/g\text{-C}_3\text{N}_4$ heterojunctions (XPS spectra) further testified the transfer of e^- from $g\text{-C}_3\text{N}_4$ (electron-rich) to V_2C MXene (electron-deficient). The e^- trapping centre was established within $V_2C/g\text{-C}_3\text{N}_4$ heterojunctions, ascribed to the difference in the work function and the band alignment, generating a built-in internal electric field.⁵¹ V_2C MXene as cocatalyst with higher metallic electrical conductivity coupled with $g\text{-C}_3\text{N}_4$ would accept the electrons, leading to less recombination of electron–hole pairs. Moreover, the heterojunctions caused charge redistribution, hindering the backward flow of e^- at the V_2C MXene from returning to $g\text{-C}_3\text{N}_4$ and recombining with h^+ . Therefore, more reactions with protons occurred to degrade dye molecules because of the more available e^- at the reduction sites. This was one of the most important reason to enhance the photocatalytic activity after coupling with V_2C MXene, which was determined by the PL peak depression in $V_2C/g\text{-C}_3\text{N}_4$ heterojunctions.⁵¹ The h^+ at VB



Scheme 2 Photocatalytic degradation mechanism by $V_2C/g\text{-C}_3\text{N}_4$ heterojunction under visible light.

reacted with water (oxidation reaction) to produce protons and oxygen. Notably, with the increase of recombination rates of e^- and h^+ , the number of available e^- and h^+ participating in redox reactions is reduced.

On the other hand, (E-13) and (E-14) expounded the production of $\cdot\text{OH}$. Specifically, O_2 was sequentially reduced and protonated by e^- at the CB of $g\text{-C}_3\text{N}_4$. The negative CB of $g\text{-C}_3\text{N}_4$ donated e^- to capture O_2 and reduce them to superoxide anion ($\cdot\text{O}_2^-$). Then, $\cdot\text{O}_2^-$ were protonated by H^+ to generate $\cdot\text{HO}_2^-$ and decomposed by e^- to give $\cdot\text{OH}$. These photo-generated electrons ($\cdot\text{OH}$, $\cdot\text{HO}_2^-$ and $\cdot\text{O}_2^-$) would react with dye molecules (CV, RhB, MB) to finally produce CO_2 and $\cdot\text{OH}$.



4. Conclusions

In summary, the V_xG_y heterojunctions were synthesized through a one-pot method. The as-prepared V_xG_y heterojunctions exhibited excellent capacity for remedying water pollution. The adsorption ratios of V_1G_5 heterojunctions onto CV and RhB (25 mg L^{-1} , $\text{pH} = 7$) were as high as 99.6% and 94%, respectively, within 170 min at room temperature in dark

environment. After adsorbing for 50 min, the dye solution equipped with V_xG_y heterojunctions was exposed to visible light for 30 min (the intensity of light irradiation was 100 W m^{-2}), displaying the final removal ratio onto CV, RhB and MB of 99.5%, 99.5%, and 95%, respectively, which is much higher than that of the published works under such low intensity of light irradiation.^{65–69} The results of DRS, PL, and band structure illustrated that the metal-like nature of V_2C MXene as a mediator coupled with $g\text{-C}_3\text{N}_4$ dramatically accelerated the separation of photogenerated charge carriers and alleviated the photogenerated recombination e^-h^+ pairs. In addition, the extraordinary 2D/2D heterojunction structure showed high charge separation capacity, which remarkably advanced the efficiency of electron/hole pair separation and transfer within V_xG_y heterojunctions. The one-pot approach to fabricate the 2D V_2C MXene/2D $g\text{-C}_3\text{N}_4$ nanosheet heterojunctions proposed in this paper provides a new idea to synthesize high-efficiency composite photocatalysts, which is significant for purifying dye wastewater.

Data availability

The data supporting this article are available from the corresponding author upon reasonable request. The data supporting this article have been included as part of the ESI.†

Author contributions

Conceptualization: Shishan Xue, Dengliang He, Shuxin Liu, Ning Chen; data curation: Herong Zhang, Yuning Zhang, Yu Wang, Yurong Zeng; funding acquisition: Shishan Xue, Shuxin Liu, Ning Chen; investigation: Yu Wang, Yurong Zeng, Herong Zhang; project administration: Shishan Xue, Dengliang He; writing – original draft: Shishan Xue, Dengliang He; writing – review & editing: Shishan Xue, Dengliang He.

Conflicts of interest

There are no conflicts to declare.

Acknowledgements

This work was financial supported by Open Fund of Vanadium and Titanium Resource Comprehensive Utilization Key Laboratory of Sichuan Province (2023FTSZ02), Mianyang Teachers' College Start-up Funding (71/QD2021A11), Innovation Team of Mianyang Teachers' College (CXTD2023PY06) and Natural Science Foundation project of Sichuan Province (2022NSFSC0201). The authors also appreciate echeshi (www.eceshi.cn) for the XRD, XPS, DRS, Zeta Potential, Raman Spectroscopy and PL tests.

Notes and references

- 1 Y. C. Yang, Q. L. Zhu, X. W. Peng, J. J. Sun, C. Li, X. M. Zhang, H. Zhang, J. B. Chen, X. F. Zhou, H. B. Zeng and Y. L. Zhang, *Environ. Chem. Lett.*, 2022, **20**, 2665.
- 2 J. H. Yan and K. Li, *Sep. Purif. Technol.*, 2021, **277**, 119469.
- 3 A. Tkaczyk, K. Mitrowska and A. Posyniak, *Sci. Total Environ.*, 2020, **717**, 137222.
- 4 C. B. Godiya, L. A. Martins Ruotolo and W. Cai, *J. Mater. Chem. A*, 2020, **8**, 21585.
- 5 K. Wang, T. Wei, Y. Li, L. He, Y. Lv, L. Chen, A. Ahmad, Y. Xu and Y. Shi, *Chem. Eng. J.*, 2021, **413**, 127410.
- 6 R. Z. Xu, G. Y. Wei, Z. M. Xie, S. J. Diao, J. F. Wen, T. Tang, L. Jiang and M. Li, *J. Alloys Compd.*, 2024, **970**, 172656.
- 7 N. Shehzad, M. Tahir, K. Johari, T. Murugesan and M. Hussain, *J. CO2 Util.*, 2018, **26**, 98.
- 8 M. Wang, Z. Cui, M. Yang, L. Lin, X. Chen, M. Wang and J. Han, *J. Colloid Interf. Sci.*, 2019, **544**, 1.
- 9 J. Ning, J. Zhang, R. Dai, Q. Wu, L. Zhang, W. Zhang, J. Yan and F. Zhang, *Appl. Surf. Sci.*, 2022, **579**, 152219.
- 10 Y. Wang, G. Tan, T. Liu, Y. Su, H. Ren, X. Zhang, A. Xia, L. Lv and Y. Liu, *Appl. Catal., B*, 2018, **234**, 37.
- 11 Q. Cao, B. Kumru, M. Antonietti and B. V. K. J. Schmidt, *Mater. Horiz.*, 2020, **7**, 762.
- 12 X. C. Wang, K. Maeda, A. Thomas, K. Takanabe, G. Xin, J. M. Carlsson, K. Domen and M. Antonietti, *Nat. Mater.*, 2009, **8**, 76.
- 13 P. Niu, L. L. Zhang, G. Liu and H. M. Cheng, *Adv. Funct. Mater.*, 2012, **22**, 4763.
- 14 M. Mohammed, A. Zakaria and A. Abdallah, *ACS Nano*, 2020, **14**, 12390.
- 15 F. Ding, D. Yang, Z. W. Tong, Y. H. Nan, Y. J. Wang, X. Y. Zou and Z. Y. Jiang, *Environ. Sci.: Nano*, 2017, **4**, 1455.
- 16 J. G. Cui, D. W. Qi and X. Wang, *Ultrason. Sonochem.*, 2018, **48**, 181.
- 17 Q. Y. Lin, L. Li, S. J. Liang, M. H. Liu, J. H. Bi and L. Wu, *Appl. Catal., B*, 2015, **163**, 135.
- 18 J. Wan, C. C. Pu, R. M. Wang, E. Z. Liu, X. Du, X. Bai, J. Fan and X. Y. Hu, *Int. J. Hydrogen Energy*, 2018, **43**, 7007.
- 19 J. X. Low, J. G. Yu, M. Jaroniec, S. Wageh and A. A. Ghamdi, *Adv. Mater.*, 2017, **29**, 1601694.
- 20 J. W. Fu, J. G. Yu, C. J. Jiang and B. Chen, *Adv. Energy Mater.*, 2018, **8**, 1701503.
- 21 Z. R. Zhu, H. W. Xia, H. Li and S. L. Han, *Inorganics*, 2022, **10**, 131.
- 22 H. J. Zhao, Y. Zhou, R. J. Wu, Z. B. Han, X. Li and Z. Yu, *Korean J. Chem. Eng.*, 2023, **40**, 3068.
- 23 M. Tahir and B. Tahir, *Chem. Eng. J.*, 2020, **400**, 125868.
- 24 S. Venkateshalu and A. N. Grace, *Appl. Mater. Today*, 2020, **18**, 100509.
- 25 A. Sheeeyna, M. Tahir and Z. Y. Zakaria, *Int. J. Hydrogen Energy*, 2024, **51**, 1511.
- 26 M. Tahir, *Energy Fuels*, 2023, **37**, 10615.
- 27 Q. Deng, F. Zhou, B. Qin, Y. Feng and Z. Xu, *Ceram. Int.*, 2020, **46**, 27326.
- 28 Z. Wang, X. Li, J. Zhou, P. Liu, Q. Huang, P. Ke and A. Wang, *J. Alloys Compd.*, 2016, **661**, 476.
- 29 A. Akhundi, A. Badiei, G. M. Ziarani, A. Habibi-Yangjeh, M. J. Munoz-Batista and R. Luque, *Mol. Catal.*, 2020, **488**, 110902.
- 30 Z. Wang, K. Yu, Y. Feng, R. Qi, J. Ren and Z. Zhu, *ACS Appl. Mater. Interfaces*, 2019, **47**, 44282.

- 31 Y. Chen, H. Yao, F. Kong, H. Tian, G. Meng, S. Wang, X. Mao, X. Cui, X. Hou and J. Shi, *Appl. Catal., B*, 2021, **297**, 120474.
- 32 F. Han, S. J. Luo, L. Y. Xie, J. J. Zhu, W. Wei, X. Chen, F. W. Liu, W. Chen, J. L. Zhao, L. Dong, K. Yu, X. R. Zeng, F. Rao, L. Wang and Y. Huang, *ACS Appl. Mater. Interfaces*, 2019, **11**, 8443.
- 33 G. G. Zhang, J. S. Zhang, M. W. Zhang and X. C. Wang, *J. Mater. Chem.*, 2012, **22**, 8083.
- 34 Y. Wang, W. Xu, Y. Zhang, Y. Z. Wu, Z. K. Wang, L. Fu, F. L. Bai, B. Y. Zhou, T. T. Wang, L. Cheng, J. Z. Shi, H. Liu and R. S. Yang, *Nano Energy*, 2021, **83**, 105783.
- 35 M. Madi, M. Tahir and Z. Y. Zakaria, *J. CO2 Util.*, 2022, **65**, 102238.
- 36 Y. Q. Shi, S. H. Jiang, K. Q. Zhou, C. L. Bao, B. Yu, X. D. Qian, B. B. Wang, N. N. Hong, P. Y. Wen, Z. Gui, Y. Hu and R. K. K. Yuen, *ACS Appl. Mater. Interfaces*, 2014, **6**, 429.
- 37 C. X. Wu, S. F. Lu, J. Zhang and Y. Xiang, *Phys. Chem. Chem. Phys.*, 2018, **20**, 7694.
- 38 F. F. Liu, J. Zhou, S. W. Wang, B. X. Wang, C. Shen, L. B. Wang, Q. K. Hu, Q. Huang and A. G. Zhou, *J. Electrochem. Soc.*, 2017, **164**, A709.
- 39 R. R. Ikreedeegh and M. Tahir, *J. Environ. Chem. Eng.*, 2021, **9**, 105600.
- 40 J. J. Chen, Z. Y. Mao, L. X. Zhang, D. J. Wang, R. Xu, L. J. Bie and B. D. Fahlman, *ACS Nano*, 2017, **11**, 12650.
- 41 J. Z. Jiang, L. Ou-yang, L. H. Zhu, A. M. Zheng, J. Zhou, X. F. Yi and H. Q. Tang, *Carbon*, 2014, **80**, 213.
- 42 B. Kumru, J. Barrio, J. R. Zhang, M. Antonietti, M. Shalom and B. V. K. J. Schmidt, *ACS Appl. Mater. Interfaces*, 2019, **11**, 9463.
- 43 B. Tahir, M. Tahir and M. G. M. Nawawi, *J. Alloys Compd.*, 2022, **927**, 166908.
- 44 X. Wang, S. Lin, H. Y. Tong, Y. N. Huang, P. Tong, B. C. Zhao, J. M. Dai, C. H. Liang, H. Wang, X. B. Zhu, Y. P. Sun and S. X. Dou, *Electrochim. Acta*, 2019, **307**, 414.
- 45 H. Y. Ding, D. L. Han, Y. J. Han, Y. Q. Liang, X. M. Liu, Z. Y. Li, S. L. Zhu and S. L. Wu, *J. Hazard. Mater.*, 2020, **393**, 122423.
- 46 M. Wu, Y. He, L. B. Wang, Q. X. Xia and A. G. Zhou, *J. Adv. Ceram.*, 2020, **9**, 749.
- 47 V. G. Parale, T. Kim, V. D. Phadtare, H. M. Yadav and H. H. Park, *J. Mol. Liq.*, 2019, **277**, 424.
- 48 M. F. Hou, C. X. Ma, W. D. Zhang, X. Y. Tang, Y. N. Fan and H. F. Wan, *J. Hazard. Mater.*, 2011, **186**, 1118.
- 49 X. Q. Xie, M. Q. Zhao, B. Anasori, K. Maleski, C. E. Ren, J. W. Li, B. W. Byles, E. Pomerantseva, G. X. Wang and Y. Gogotsi, *Nano Energy*, 2016, **26**, 513.
- 50 J. N. Guo, J. M. Zhou, Z. Sun, M. Y. Wang, X. Y. Zou, H. L. Mao and F. Yan, *Acta Biomater.*, 2022, **146**, 70.
- 51 D. Huang, Y. Xie, D. Lu, Z. Wang, J. Wang, H. Yu and H. Zhang, *Adv. Mater.*, 2019, **31**, 1901117.
- 52 A. Sherryna, M. Tahir and Z. Y. Zakaria, *Int. J. Hydrogen Energy*, 2024, **51**, 1511.
- 53 X. Jiang, A. V. Kuklin, A. Baev, Y. Ge, H. Ågren, H. Zhang and P. N. Prasad, *Phys. Rep.*, 2020, **848**, 1.
- 54 V. N. Khabashesku, J. L. Zimmerman and J. L. Margrave, *Chem. Mater.*, 2000, **12**, 3264.
- 55 X. Bao, H. Li, Z. Wang, F. Tong, M. Liu, Z. Zheng, P. Wang, H. Cheng, Y. Liu, Y. Dai, Y. Fan, Z. Li and B. Huang, *Appl. Catal., B*, 2021, **286**, 119885.
- 56 M. Dan, S. Yu, W. H. Lin, M. Abdellah, Z. Guo, Z. Q. Liu, T. Pullerits, K. B. Zheng and Y. Zhou, *Adv. Mater.*, 2024, **2415138**.
- 57 M. Dan, J. Li, C. Chen, J. Xiang, Y. Zhong, F. Wu, Z. Wang, Z. Q. Liu and Y. Zhou, *Energy Technol.*, 2022, **10**, 2100188.
- 58 B. Li, H. Song, F. Han and L. Wei, *Appl. Catal., B*, 2020, **269**, 118845.
- 59 M. Dan, J. Xiang, J. Yang, F. Wu, C. Han, Y. Zhong, K. Zheng, S. Yu and Y. Zhou, *Appl. Catal., B*, 2021, **284**, 119706.
- 60 M. Dan, F. Wu, J. Xiang, Y. Cao, Y. Zhong, K. Zheng, Y. Liu, Z. Q. Liu, S. Yu and Y. Zhou, *Chem. Eng. J.*, 2021, **423**, 130201.
- 61 W. S. Ai, C. F. Zhang, L. Xia, H. Miao and J. L. Yuan, *Energies*, 2022, **15**, 3696.
- 62 H. Lei, Z. D. Hao, K. Chen, Y. H. Chen, J. N. Zhang, Z. J. Hu, Y. J. Song, P. H. Rao and Q. Huang, *J. Phys. Chem. Lett.*, 2020, **11**, 4253.
- 63 C. Wu, W. Huang, H. Liu, K. Lv and Q. Li, *Appl. Catal., B*, 2023, **330**, 122653.
- 64 Q. Lin, G. Zeng, S. Pu, G. Yan, J. Luo, Y. Wan and Z. Zhao, *Chem. Eng. J.*, 2022, **443**, 136335.
- 65 J. Wang, L. Z. Ren, D. E. Zhang, X. Y. Hao, J. Y. Gong, X. Xiao, Y. X. Jiang and Z. W. Tong, *J. Mater. Res.*, 2018, **33**, 3928.
- 66 J. J. Zhao, T. Y. Guo, H. T. Wang, M. F. Yan and Y. Qi, *J. Alloys Compd.*, 2023, **947**, 169613.
- 67 H. G. Liang, J. B. Zhao, A. Brouzgou, A. H. Wang, S. Y. Jing, P. Kannan, F. Chen and P. Tsiakaras, *Sep. Purif. Technol.*, 2025, **677**, 1120.
- 68 A. S. Vig, A. Gupta and O. P. Pandey, *Adv. Powder Technol.*, 2018, **29**, 2231.
- 69 R. Rangel, V. Cedeño, J. Espino, P. B. Pérez, G. R. Gattorno and J. A. Gil, *Catalysts*, 2018, **8**, 668.